ARL-TR-9992 ● Oct 2024

Improved Yttria-Stabilized Zirconia (YSZ) and Rare Earth Oxide (REO) Blends: Processability and Calcia–Magnesia–Alumina–Silicate Response

by Clara Mock, Andrew Wright, Nickolas Sotiropoulos, Timothy Sharobem, Chris Dambra, Brian Keyes, and Anindya Ghoshal

NOTICES

Disclaimers

The findings in this report are not to be construed as an official Department of the Army position unless so designated by other authorized documents.

Citation of manufacturer's or trade names does not constitute an official endorsement or approval of the use thereof.

Destroy this report when it is no longer needed. Do not return it to the originator.

ARL-TR-9992 ● OCT 2024

Improved Yttria-Stabilized Zirconia (YSZ) and Rare Earth Oxide (REO) Blends: Processability and Calcia–Magnesia–Alumina–Silicate Response

Clara Mock and Anindya Ghoshal
DEVCOM Army Research Laboratory

Andrew Wright
Oak Ridge Associated Universities

Nickolas Sotiropoulos
SURVICE Engineering

Timothy Sharobem, Chris Dambra, and Brian Keyes
Oerlikon Metco

REPORT DOCUMENTATION PAGE

1. REPORT DATE	2. REPORT TYPE	3. DATES COVERED	
		START DATE	END DATE
October 2024	Technical Report	October 2020	August 2024

4. TITLE AND SUBTITLE
Improved Yttria-Stabilized Zirconia (YSZ) and Rare Earth Oxide (REO) Blends: Processability and Calcia–Magnesia–Alumina–Silicate Response

5a. CONTRACT NUMBER	5b. GRANT NUMBER	5c. PROGRAM ELEMENT NUMBER
5d. PROJECT NUMBER	**5e. TASK NUMBER**	**5f. WORK UNIT NUMBER**

6. AUTHOR(S)
Clara Mock, Andrew Wright, Nickolas Sotiropoulos, Timothy Sharobem, Chris Dambra, Brian Keyes, and Anindya Ghoshal

7. PERFORMING ORGANIZATION NAME(S) AND ADDRESS(ES)	8. PERFORMING ORGANIZATION REPORT NUMBER
DEVCOM Army Research Laboratory ATTN: FCDD-RLA-MD Aberdeen Proving Ground, MD 21005	ARL-TR-9992

9. SPONSORING/MONITORING AGENCY NAME(S) AND ADDRESS(ES)	10. SPONSOR/MONITOR'S ACRONYM(S)	11. SPONSOR/MONITOR'S REPORT NUMBER(S)

12. DISTRIBUTION/AVAILABILITY STATEMENT
DISTRIBUTION STATEMENT A. Approved for public release: distribution unlimited.

13. SUPPLEMENTARY NOTES
ORCIDs: Clara Mock, 0000-0001-8055-2371; Anindya Ghoshal, 0000-0001-6338-1224

14. ABSTRACT
There is a need for the development of tough, mechanically robust coatings resistant to calcia–magnesia–alumina–silicate (CMAS) glass attack for turboshaft gas turbine engine applications. Previously, an yttria-stabilized zirconia (YSZ) with gadolinium oxide (Gd_2O_3) composite coating was developed where the CMAS delaminated without infiltrating or forming reaction products. This coating was difficult to process due to poor flowability of the blended YSZ and Gd_2O_3 powders. A spray-drying and sintering route was used to develop readily processable YSZ rare-earth oxide (REO) mixed powders (where the REO was Gd_2O_3, samarium oxide [Sm_2O_3], cerium oxide [CeO_2], and hafnium oxide [HfO_2]) to further explore the effect of REO chemistry on CMAS behavior. Chemical reaction between the YSZ and REO formed a fluorite, (REO, Zr)O_2, phase for all mixtures except the YSZ–HfO_2 powder and coating. Characterization of the powders and air plasma spray coatings is included, as well as a discussion on the effect of REO chemistry on CMAS wettability behavior.

15. SUBJECT TERMS
calcia–magnesia–alumina–silicate, air plasma spray, thermal barrier coatings, rare-earth oxide, yttria-stabilized zirconia, Mechanical Sciences, Sciences of Extreme Materials

16. SECURITY CLASSIFICATION OF:			17. LIMITATION OF ABSTRACT	18. NUMBER OF PAGES
a. REPORT	b. ABSTRACT	C. THIS PAGE		
UNCLASSIFIED	UNCLASSIFIED	UNCLASSIFIED	UU	30

19a. NAME OF RESPONSIBLE PERSON	19b. PHONE NUMBER *(Include area code)*
Clara Mock	(410) 306-0821

STANDARD FORM 298 (REV. 5/2020)
Prescribed by ANSI Std. Z39.18

Contents

List of Figures

List of Tables

Acknowledgments

This research was funded by Strategic Environmental Research and Development Program (SERDP) as part of the Sandphobic Thermal/Environmental Barrier Coatings for Gas Turbine Engines Project under agreement number WP20-C3-1281.

Research was sponsored by the US Army Combat Capabilities Development Command (DEVCOM) Army Research Laboratory (ARL) and was accomplished under Cooperative Agreement Number W911NF-21-2-0066. The views and conclusions contained in this document are those of the authors and should not be interpreted as representing the official policies, either expressed or implied, of ARL or the US Government. The US Government is authorized to reproduce and distribute reprints for Government purposes notwithstanding any copyright notation herein.

The research reported in this document was performed in connection with contract/instrument W911QX-16-D-0014 with ARL. The views and conclusions contained in this document are those of SURVICE Engineering and ARL. Citation of manufacturer's or trade names does not constitute an official endorsement or approval of the use thereof. The US Government is authorized to reproduce and distribute reprints for Government purposes notwithstanding any copyright notation here.

1. Introduction

Thermal barrier coatings have long been used to extend the service temperatures of components in the hot section of gas turbine engines.[1,2] These coatings are susceptible to damage when flying in ash- or sand-laden environments. Ingested ash or sand melts and forms calcia–magnesia–alumina–silicate (CMAS) glass when it enters the hot section of the gas turbine engine, causing CMAS buildup on components and/or causing coating exfoliation.[3] Rare-earth oxides (REOs) react with CMAS, potentially suppressing infiltration and, therefore, could be used to protect and extend the life of thermal barrier coatings.[4–7] Rare-earth-based solutions, like gadolinium zirconate, can suffer from poor mechanical properties such as low fracture toughness and poor erosion resistance.[8,9]

In previous work, the authors mechanically blended yttria-stabilized zirconia (YSZ) with gadolinium oxide (Gd_2O_3) powder and deposited it as a coating with air plasma spray (APS) to create a banded composite structure with discrete layers of YSZ and Gd_2O_3.[10] The idea was to combine the excellent strength and toughness of YSZ with the CMAS resistance of Gd_2O_3. A range of blends from 2 to 32 vol% Gd_2O_3 were tested and found that increasing the Gd_2O_3 ratio decreased the adhesion of CMAS to the coating. At 32 vol% Gd_2O_3, the CMAS completely delaminated from the coating, although significant CMAS buildup was noted. The powders from that study were mechanically mixed and had powder particle sizes with poor flowability (i.e., poor processability) for APS, which limits scale-up and industrial application of this coating. In addition, the use of YSZ mixed with other REOs could potentially have additional CMAS-resistant qualities that are of interest. To improve processability, powders were spray-dried and sintered as a composite YSZ–REO particulate with an appropriate size distribution for APS. The experimental powders consisted of YSZ mixed with Gd_2O_3, cerium oxide (CeO_2), samarium oxide (Sm_2O_3), and hafnium oxide (HfO_2), respectively. The powders and coating were characterized, and CMAS behavior in the form of contact angle measurements is discussed.

2. Experimental

Powders were manufactured at Oerlikon Metco (Westbury, NY). A NiCoCrAl (Amdry 365-2) commercial powder was used as the bond coat for all topcoat depositions. A commercially available YSZ (Metco 204NS) powder was used as the baseline for comparison. Four experimental powders were examined in this study which were a mixture of YSZ and 30 vol% REO, where the REO was either CeO_2, Sm_2O_3, Gd_2O_3, or HfO_2. A 30 vol% REO to 70 vol% YSZ was targeted based

on previous work with Gd_2O_3, which exhibited enhanced CMAS resistance at 32 vol% compared to lower REO concentrations.[10] The powders were produced through a combination of milling, spray drying, and sintering to improve cohesion of each powder particle. Table 1 is a list of the chemistries for each ceramic powder that was used as a topcoat in this study.

Table 1 Chemistry of topcoat powders

ID	ZrO_2 (wt%)	Y_2O_3 (wt%)	REO	REO (wt%)
YSZ	92–93	7–8	N/A	N/A
YSZ–CeO_2	60–66	4–5	CeO_2	30–35
YSZ–Sm_2O_3	55–62	3–5	Sm_2O_3	35–40
YSZ–Gd_2O_3	58–63	4–6	Gd_2O_3	33–36
YSZ–HfO_2	53–57	3–5	HfO_2	38–42

Scanning electron microscopy (SEM) of the powders loosely sprinkled onto carbon tape was completed using a Phenom XL G2 SEM (Thermo Fisher Scientific, Waltham, MA) to examine the powder size and morphology. Particle size distribution of the powders was measured with a QIQPIC RODOS/L + VIBRI/L (Sympatec GmbH, Clausthal-Zellerfeld, Germany) particle size analyzer with dynamic image analysis in dry mode. The phase of each powder was examined via X-ray diffraction (XRD) with a D2 Phaser (Bruker, Billerica, MA) equipped with a Cu source operating at 30 kV and 10 mA. The XRD spectra was collected from 20° to 90° with a step size of 0.02°, sample rotation of 15 rpm and a dwell time of 2 s per step. A Brookfield (Middleboro, MA) powder flow tester (PFT) was used to characterize the flowability of the powder using the flow function test with the 5-inch vane and trough.

To prepare the substrate for coating, Inconel 718 discs (1.0 inch diameter) were grit blasted with 60 grit aluminum oxide particles at 60 psi with a 2 in standoff for approximately 5 s. After grit blasting, the discs were ultrasonically cleaned in ethanol for 5 min and allowed to air dry. A SG-100 (Aimtek, Auburn, MA) plasma spray gun using a mixture of argon and helium gas was used to deposit all coatings. Argon was used as the powder carrier gas. Full APS processing conditions can be found in a supplementary document.[11] The as-sprayed coating surface roughness was measured with an OLS5100 confocal laser scanning microscope (Olympus, Waltham, MA). Coatings were metallographically polished to a 0.02 μm finish using colloidal silica and examined with a Hitachi SU3500 (Minato-ku, Tokyo) SEM operating in low-vacuum mode at 30 Pa. Porosity of the coatings was determined through image analysis of the coatings as imaged under SEM via a simple thresholding technique using FIJI software.[12] The coating porosity measured included areas from both voids and any microcracking. XRD of the coatings was collected using the same system and methods as described for the powder XRD.

3. Results and Discussion

3.1 Powder Characterization

The powder size distribution and morphology affect not only the flow behavior through the powder feeder to the gun but also the in-flight melt behavior of the particles through the plasma spray gun. Secondary electron (SE) SEM micrographs of the powders sprinkled onto carbon tape can be found in Fig. 1. The commercial bond coat powder, NiCoCrAl, has a uniform size distribution of spherical particles with few satellites (see Fig. 1a). The commercial YSZ powder has a wide distribution of powder particle sizes with mostly smaller particles present (see Fig. 1b). The particles are completely smooth and spherical, which is expected to lead to excellent flowability. The YSZ–CeO2 (Fig. 1c), YSZ–Sm_2O_3 (Fig. 1d), and YSZ–Gd_2O_3 (Fig. 1e) all have a larger particle size with a tighter distribution than YSZ. All powders have a smooth surface but some, especially the YSZ–CeO_2 and the YSZ–Sm_2O_3, appear to have a concave portion of the particles suggesting large internal porosity. The YSZ–HfO_2 powder shows extreme internal powder porosity such that the shape is deformed and less spherical than the others. Differences in the particle size distribution of the milled YSZ/REO powders may have caused differing spray behavior during the spray drying process resulting in the differing morphologies and porosities. A summary of the particle size for the YSZ and YSZ–REO powders is in Table 2. The YSZ–REO particle size is very similar regardless of chemistry but larger than the YSZ powder.

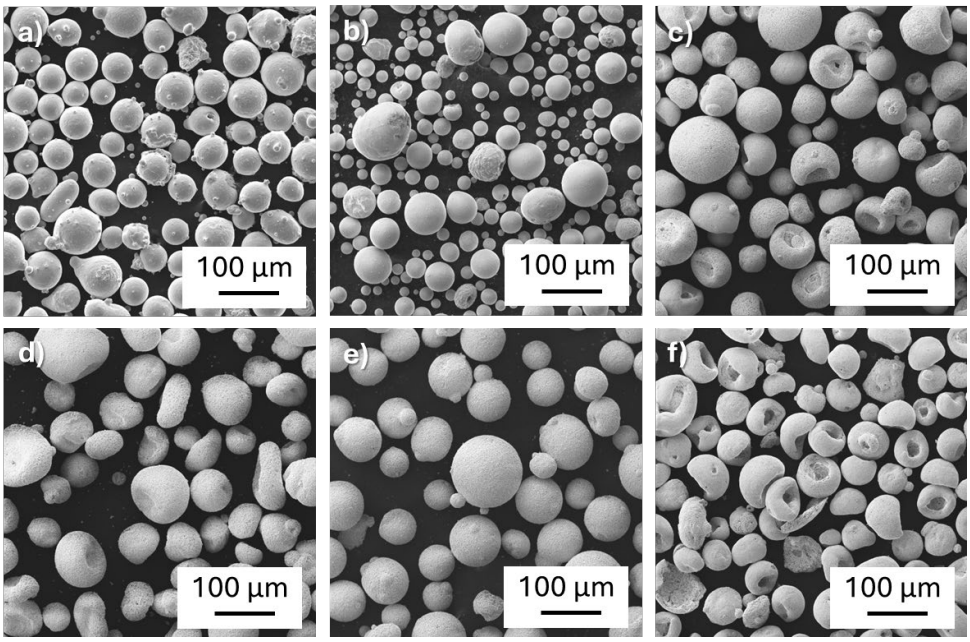

Fig. 1 SEM SE micrographs of APS powder sprinkled on carbon tape taken in SE mode: a) NiCoCrAl, b) YSZ, c) YSZ–CeO_2, d) YSZ–Sm_2O_3, e) YSZ–Gd_2O_3, and f) YSZ–HfO_2

Table 2 Particle size distribution of each oxide powder

Powder	D10 (µm)	D50 (µm)	D90 (µm)
YSZ	26.24	57.89	96.5
YSZ–CeO_2	51.5	83.01	121.95
YSZ–Sm_2O_3	50.88	82.64	132.44
YSZ–Gd_2O_3	50.48	76.72	111.79
YSZ–HfO_2	54.13	84.69	122.55

The experimental powders were examined by XRD to determine if the sintering process, used to help solidify and strengthen the powders, caused chemical changes to the YSZ–REO powders. The XRD spectrum for YSZ powder is in Fig. 2. As expected, the predominate phase is tetragonal YSZ with minor amounts of cubic Y_2O_3 and monoclinic ZrO_2 present.

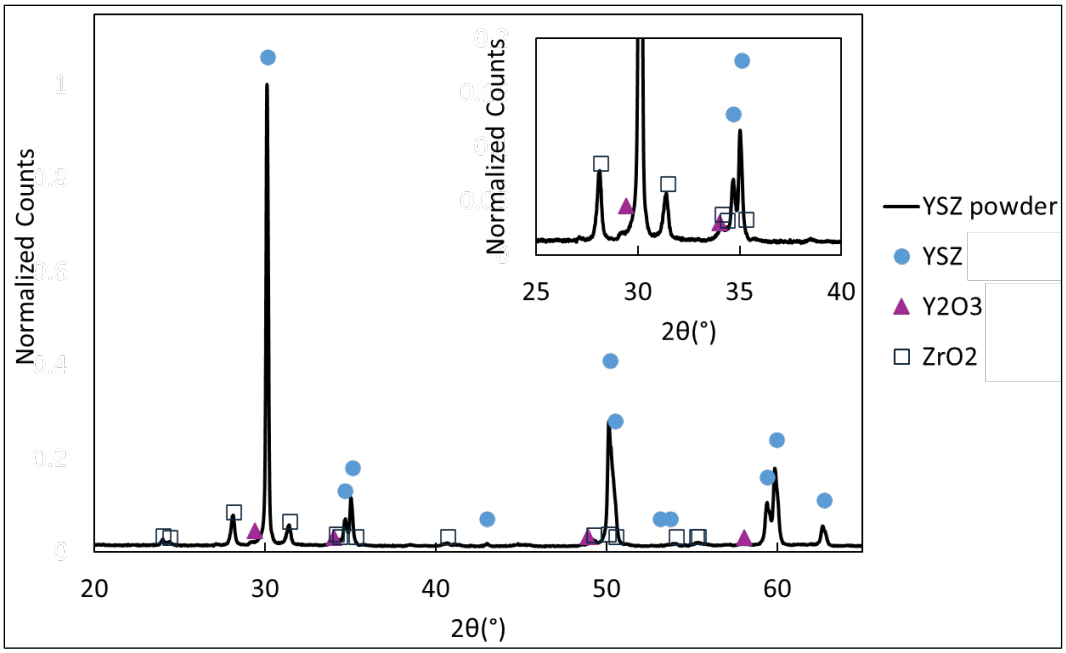

Fig. 2 XRD spectrum for YSZ powder

The YSZ–CeO_2 powder XRD spectrum is shown in Fig. 3. There are strong peaks for YSZ but the majority of the CeO_2 phase has reacted with the YSZ to form a fluorite yttrium, cerium-stabilized zirconia, although small peaks of CeO_2 can still be found in the pattern.

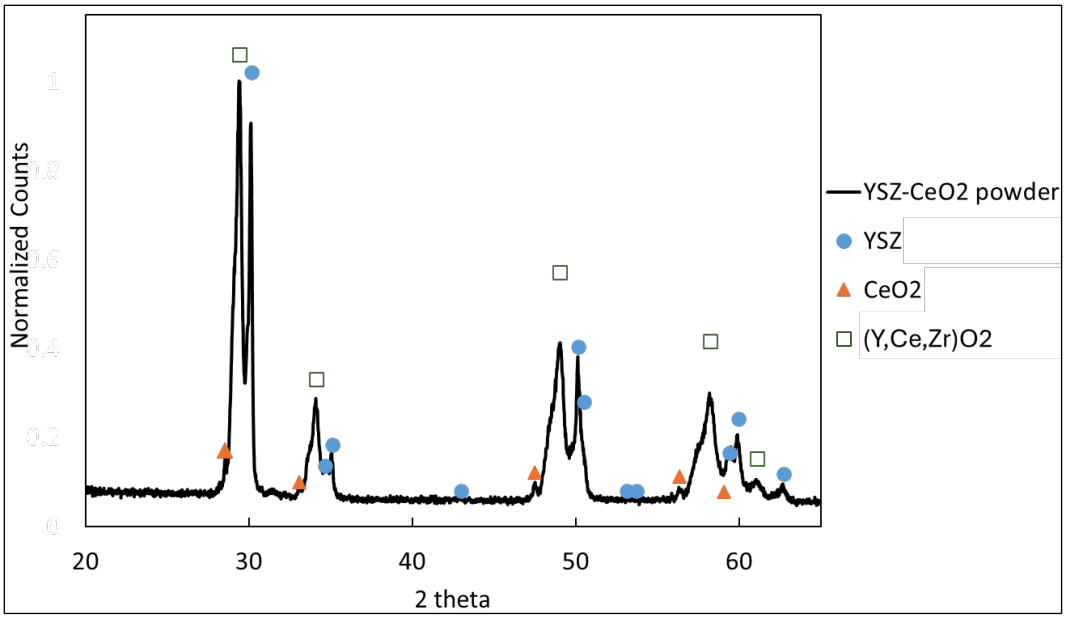

Fig. 3 XRD spectrum for YSZ–CeO2 powder

Similarly, the YSZ–Sm_2O_3 powder also reacted with the YSZ to form several phases including samarium zirconate, $Sm_2Zr_2O_7$, and a fluorite, samarium-stabilized zirconia, $(Sm,Zr)O_2$ (Fig. 4). Sm_2O_3 peaks were not found in the XRD spectrum.

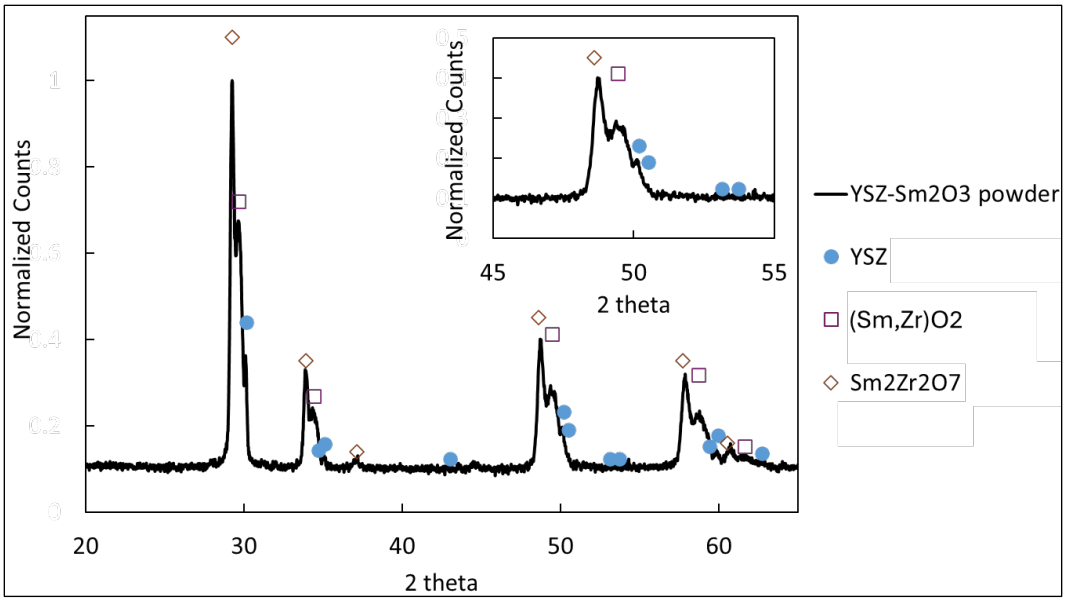

Fig. 4 XRD spectrum for YSZ–Sm_2O_3 powder

The YSZ–Gd_2O_3 powder reacted to primarily form a fluorite, gadolinium-stabilized zirconium oxide, $(Gd,Zr)O_2$, with only minor amounts of YSZ and Gd_2O_3 remaining in the powder (Fig. 5).

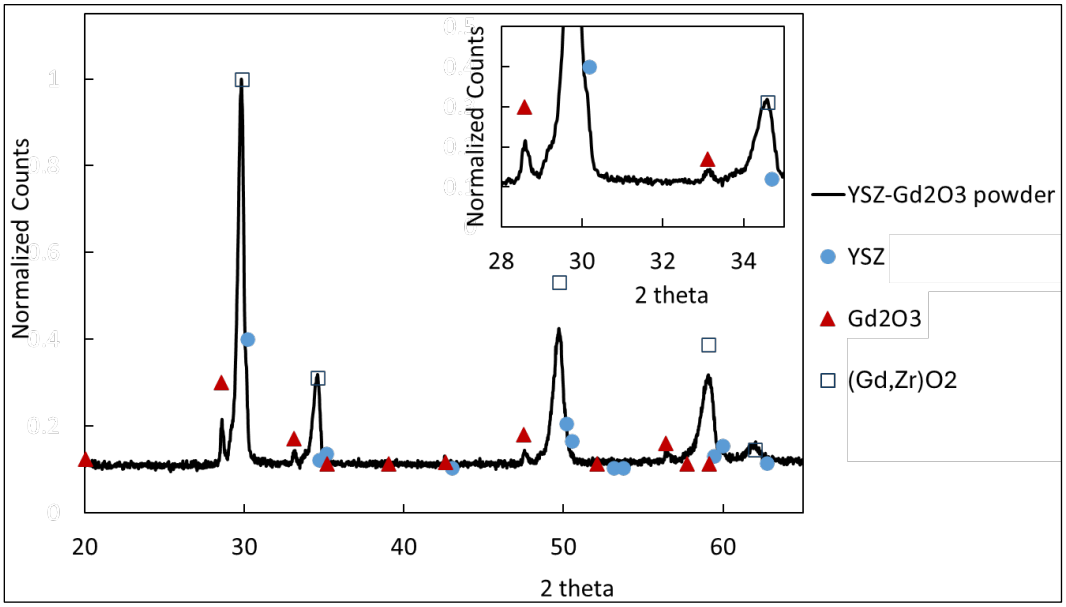

Fig. 5 XRD spectrum for YSZ–Gd_2O_3 powder

Only the YSZ–HfO_2 powder (Fig. 6) did not show any signs of alloying, with only YSZ and HfO_2 detected via XRD.

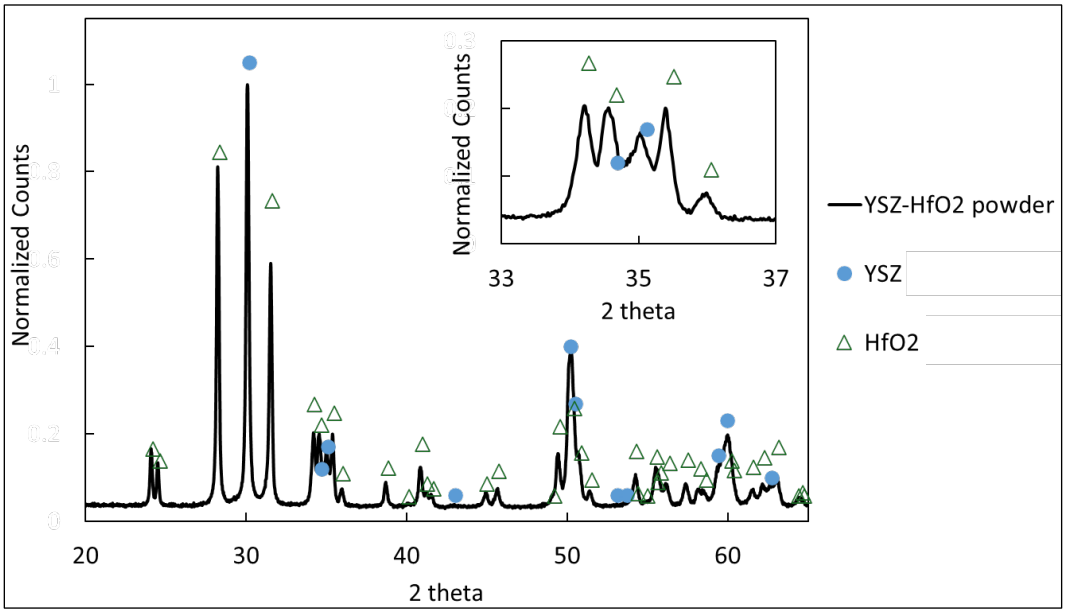

Fig. 6 XRD spectrum for YSZ–HfO_2 powder

A summary of the phases observed for all XRD spectrums is provided in Table 3. The primary phase observed in each spectrum is bolded for easy reference. In the experimental powders, all powders showed signs of YSZ–REO alloying except the YSZ–HfO_2 powder. Of the powders that reacted, only the YSZ–CeO_2 retained YSZ as a primary phase. YSZ–CeO_2 and YSZ–Gd_2O_3 both alloyed to form a fluorite, REO-stabilized zirconia, as the primary phase. YSZ–Sm_2O_3 was the only powder to form a REO-based zirconate. The powder diffraction file (PDF) chemistry for each phase identified is provided in Table 3 for reference but the specific chemistry of each phase was not determined in this study. Although the phases can and do change as a result of the APS process, it is helpful to know what is present before spraying to understand the effects of APS processing on the final chemistry.

Table 3 Summary of phases observed in each powder

Powder	Phases present	Crystal structure	Prevalence	PDF chemical formula	PDF no.
YSZ	**YSZ**	tetragonal	**primary**	Zr0.92Y0.08O1.96	00-048-0224
	Y_2O_3	cubic	minor	Y2O3	00-043-0661
	ZrO_2	monoclinic	minor	ZrO2	00-037-1484
YSZ–CeO_2	**YSZ**	tetragonal	**primary**	Zr0.92Y0.08O1.96	00-048-0224
	(Y,Ce,Zr)O_2	cubic	**primary**	Y0.21Ce0.36Zr0.43O1.89	04-020-7368
	CeO_2	cubic	minor	CeO2	00-034-0394
YSZ–Sm_2O_3	YSZ	tetragonal	minor	Zr0.92Y0.08O1.96	00-048-0224
	(Sm,Zr)O_2	cubic	moderate	Sm0.3Zr0.7O1.85	04-024-6386
	$Sm_2Zr_2O_7$	cubic	**primary**	Sm2Zr2O7	00-024-1012
YSZ–Gd_2O_3	YSZ	tetragonal	minor	Zr0.92Y0.08O1.96	00-048-0224
	Gd_2O_3	cubic	minor	Gd2O3	00-012-0797
	(Gd,Zr)O_2	cubic	**primary**	Gd0.26Zr0.74O1.87	04-017-4773
YSZ–HfO_2	**YSZ**	tetragonal	**primary**	Zr0.92Y0.08O1.96	00-048-0224
	HfO_2	monoclinic	**primary**	HfO2	00-072-0468

Note: Primary phase observed in each spectrum is bolded.

The powder flowability of the experimental YSZ–REO powders, which were spray dried and sintered, were compared with historical data for manually blended YSZ–32vol%Gd_2O_3 and YSZ–32vol%Sm_2O_3 powders. Blended YSZ with Gd_2O_3 was very difficult to process via APS due to poor powder flowability, which was limited by the fine Gd_2O_3 particle size.[10] An additional study by the authors explored blending YSZ with Sm_2O_3 but the flowability of these blends was so poor it could not be processed via APS. Both the blended YSZ–Gd_2O_3 and YSZ–Sm_2O_3 powders were tested with the PFT and the results are presented in Fig. 7. In general, powders with curves at or below the "free flowing" line in Fig. 7 are easy to process through standard thermal spray powder feeders. The flowability of the powders produced by spray drying and sintering were all at or below the "free flowing" line and, therefore, all the YSZ–REO powders were shown to be suitable for APS processing.

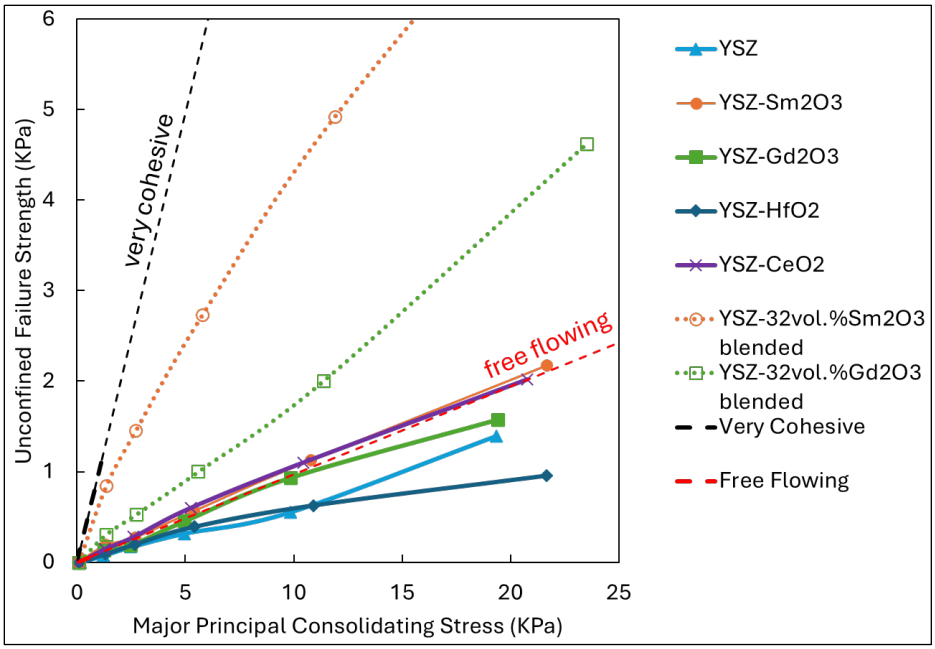

Fig. 7 Powder flowability of experimental YSZ–REO powders compared to YSZ and previously tested YSZ–REO blended powders

The primary aim of this work was to create an easier-to-process powder that was a mixture of YSZ and REO. Based on the results here, the powder was expected to be much easier to process via APS processing; however, many of the powders no longer retained the original desired chemistry. Regardless, the powders were sprayed via APS.

3.2 Coating Characterization

The coatings were characterized to understand the quality of deposition from APS processing, which included chemical analysis, surface roughness, and microstructure—all of which affect coating performance. The coating surface roughness is an important metric to measure because a high roughness will reduce engine efficiency due to reductions in the pressure ratio[13] but is also expected to influence the interaction behavior of CMAS on the coating surface. A representative height map of the YSZ-coated disc is in Fig. 8.

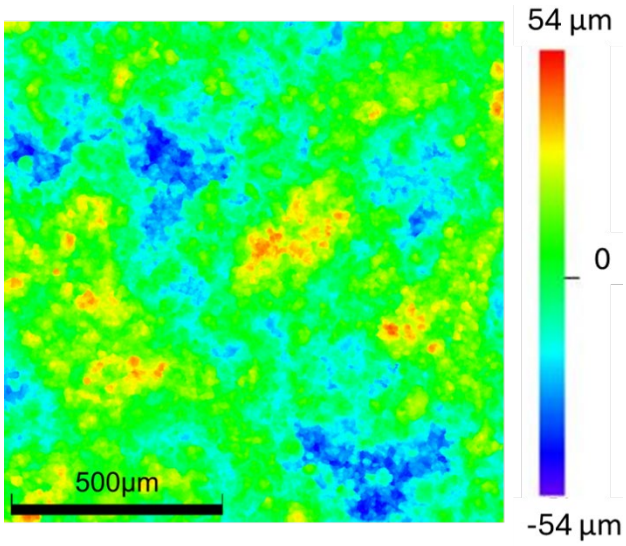

Fig. 8 Height map of YSZ-coated disc in the as-sprayed condition

All coatings shared similar morphologies where the height is generally skewed in the positive direction, indicative of an additive, deposition process with a few peaks homogenously spread throughout the coating. Table 4 compares the surface roughness for all coatings. The YSZ coating was smoother than the experimental coatings, with the YSZ–Gd_2O_3 coating having the largest S_a and S_z.

Table 4 Summary of surface roughness of the as-sprayed coatings

Sample ID	S_z (µm)	S_a (µm)
7YSZ	102.43	11.23
YSZ–CeO_2	124.41	15.46
YSZ–Gd_2O_3	151.44	17.94
YSZ–HfO_2	133.13	14.59
YSZ–Sm_2O_3	117.62	14.32

Phase and chemical changes in coatings frequently occur during APS processing from the rapid solidification of individual splats in the presence of an air atmosphere.[14] To understand the phase and chemistry changes due to APS, XRD was performed on all coatings. The YSZ coating consisted primarily of the tetragonal, YSZ, phase with minor amounts of cubic, Y_2O_3, and monoclinic, ZrO_2 (Fig. 9). The relative intensity of the Y_2O_3 and ZrO_2 peaks appear to be reduced in the coating compared to the powder indicating a more homogeneous phase.

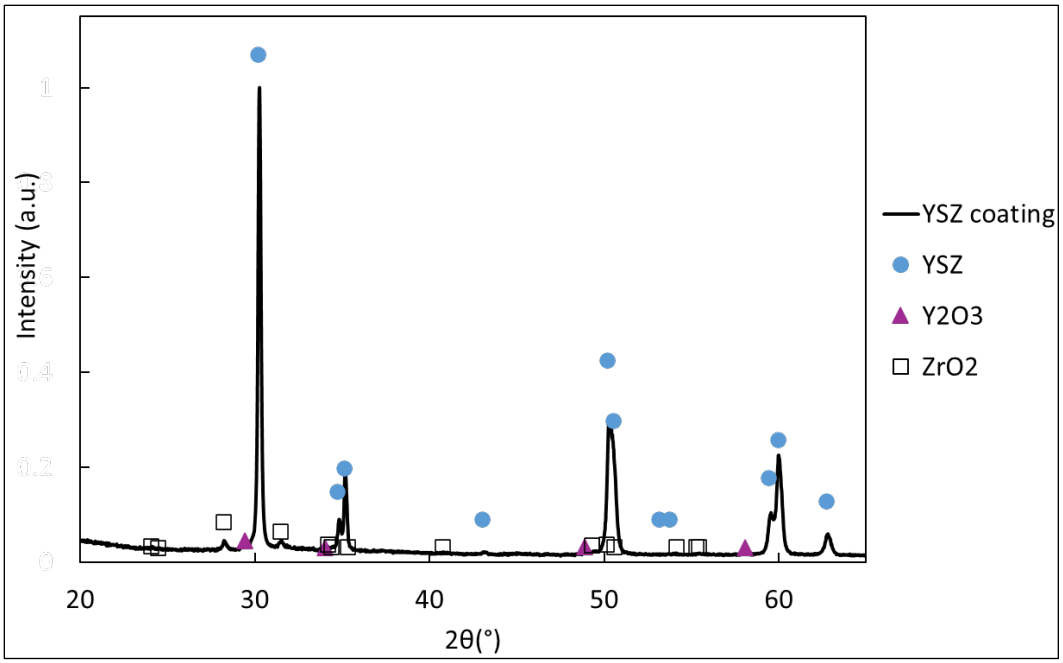

Fig. 9 XRD spectrum of YSZ coating

For the YSZ–CeO_2 coating, additional alloying occurred during APS indicated by the reduction of the YSZ peak intensity leaving the fluorite (Y,Ce,Zr)O_2 phase as the predominant phase present (Fig. 10). The CeO_2 phase is completely absent in the as-sprayed coating.

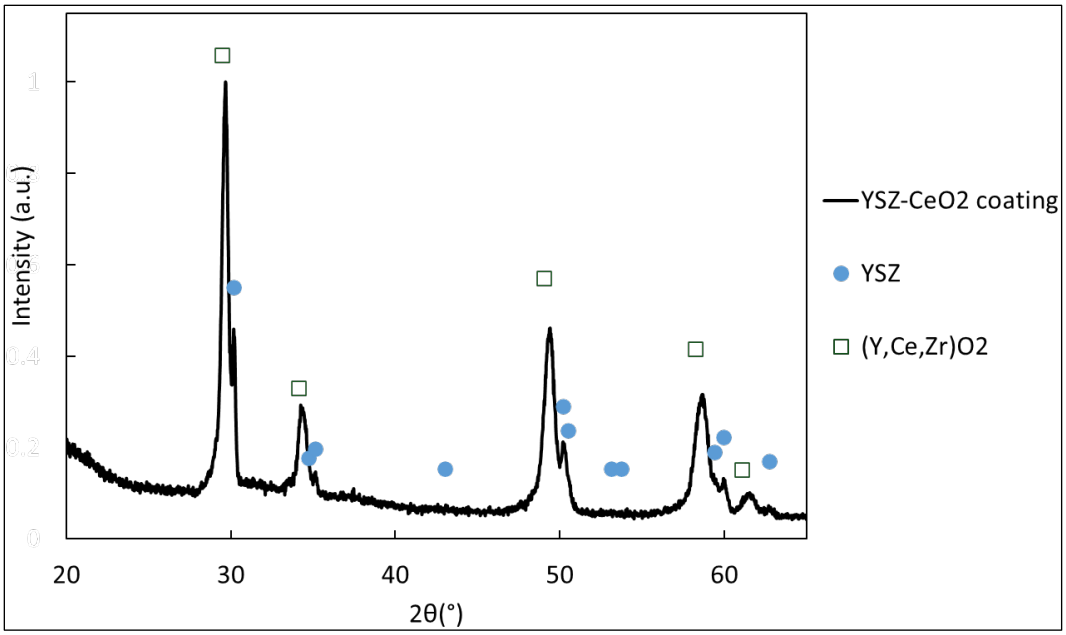

Fig. 10 XRD spectrum of YSZ–CeO_2 coating

For the YSZ–Sm_2O_3 coating, the APS process again further homogenized the powders producing a primarily fluorite, $(Sm,Zr)O_2$, phase with minor peaks of the tetragonal YSZ (Fig. 11). The $Sm_2Zr_2O_7$ phase was completely absent after APS processing.

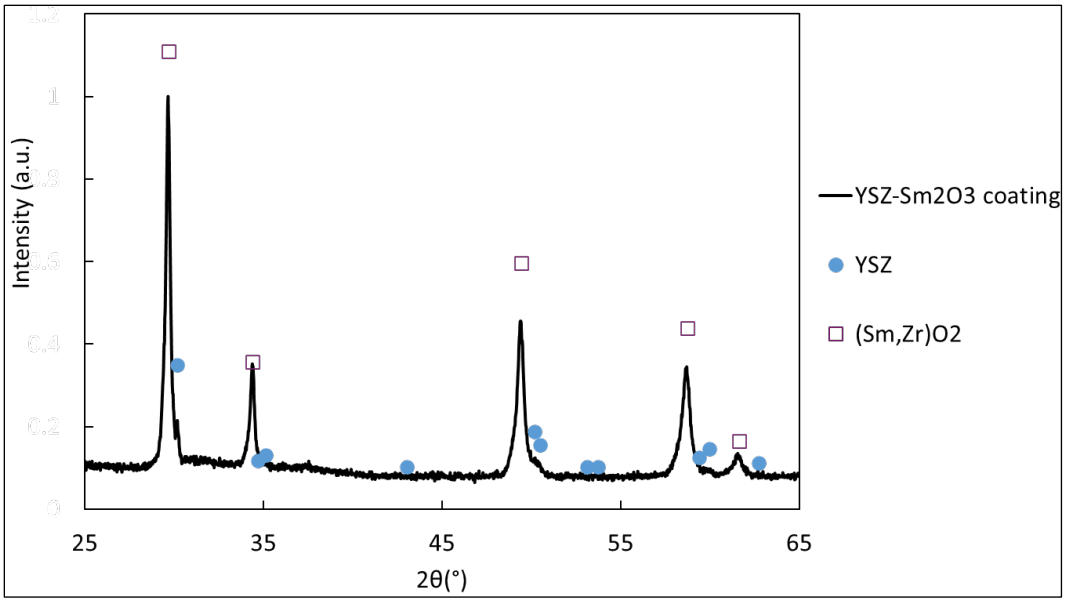

Fig. 11 XRD spectrum of the YSZ–Sm_2O_3 coating

In Fig. 12, the XRD spectrum for the YSZ–Gd_2O_3 coating shows that the primary phase is the fluorite, $(Gd,Zr)O_2$, phase with minor amounts of tetragonal YSZ. The Gd_2O_3 phase was completely alloyed into the other phases during the APS process.

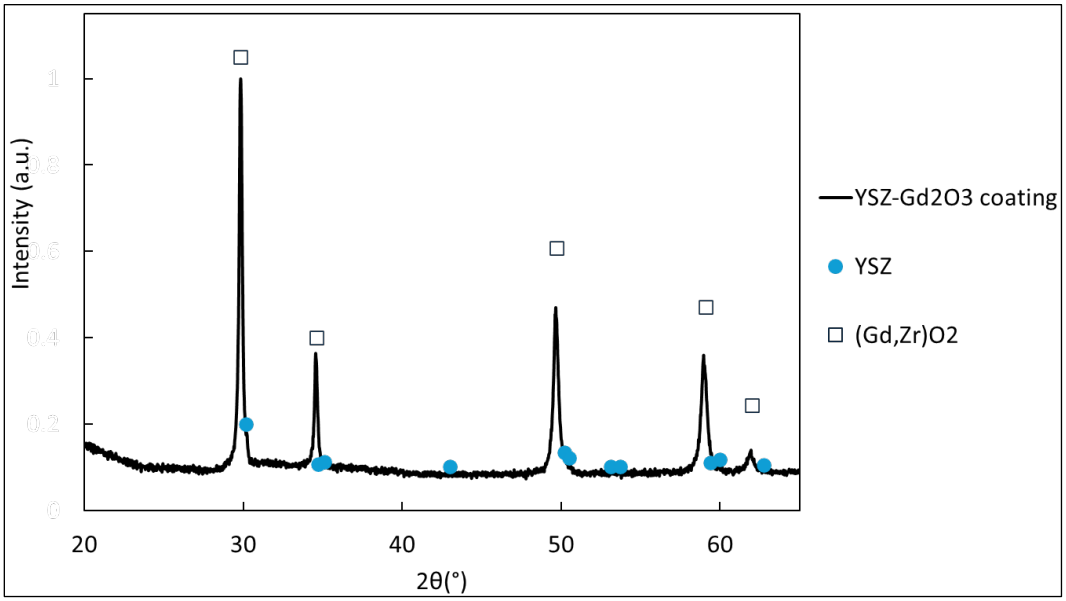

Fig. 12 XRD spectrum of the YSZ–Gd_2O_3 coating

The YSZ–HfO_2 coating was the only coating where the REO can be found in the final coating (Fig. 13); however, the REO peaks were greatly reduced after APS. It is possible that the HfO_2 volatized during APS processing. The reduction of HfO_2 REO is expected to reduce the resistance to CMAS.

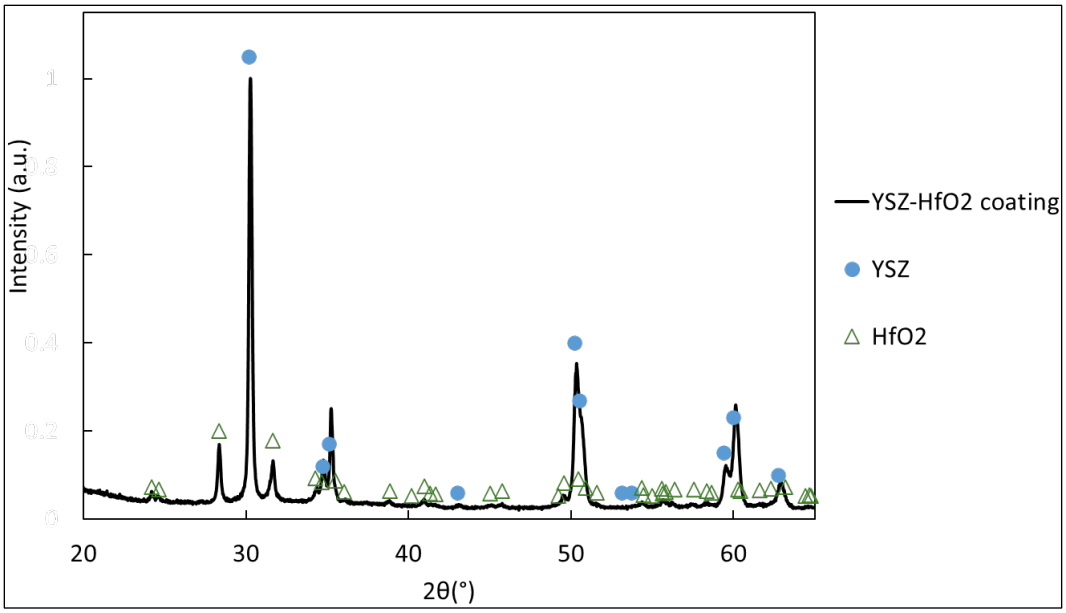

Fig. 13 XRD spectrum of the YSZ–HfO_2 coating

The chemistry of all coatings changed because of APS processing (Table 5). The YSZ coating homogenized slightly. Three of the YSZ–REO coatings reacted with the REO to form a fluorite, REO–ZrO_2, phase. It has been shown previously the YSZ and CeO_2, Sm_2O_3, or Gd_2O_3 tended to react and form the cubic, fluorite phase on the REO-rich side of the respective ZrO_2–REO phase diagram,[15,16] so it is not surprising that they are reacting here. However, it was surprising to see how quickly the phases reacted and homogenized even during APS, which is a rapid solidification process. In the original YSZ–Gd_2O_3 blended work, the coatings were heat-treated in air at 1000 °C for 100 h with little change in phase fraction.[10] It is likely that for this study, the more uniform distribution of fine REO particulates within the powder helped to accelerate interdiffusion. The authors were not able to locate a binary phase diagram for ZrO_2–HfO_2, but it appears there is less solubility between these two chemistries as they remained separate through powder and APS processing. However, the apparent significant HfO_2 loss during APS is concerning and additional APS process development may be necessary to deposit and retain this chemistry in future coatings.

Table 5 Summary of coating XRD results

Coating	Phases present	Crystal structure	Occurrence	PDF chemical formula	PDF no.
YSZ	**YSZ**	tetragonal	**primary**	Zr0.92Y0.08O1.96	00-048-0224
	Y_2O_3	cubic	minor	Y2O3	00-043-0661
	ZrO_2	monoclinic	minor	ZrO2	00-037-1484
YSZ–CeO_2	YSZ	tetragonal	minor	Zr0.92Y0.08O1.96	00-048-0224
	(Y,Ce,Zr)O_2	cubic	**primary**	Y0.21Ce0.36Zr0.43O1.89	04-020-7368
YSZ–Sm_2O_3	YSZ	tetragonal	minor	Zr0.92Y0.08O1.96	00-048-0224
	(Sm,Zr)O_2	cubic	**primary**	Sm0.3Zr0.7O1.85	04-024-6386
YSZ–Gd_2O_3	YSZ	tetragonal	minor	Zr0.92Y0.08O1.96	00-048-0224
	(Gd,Zr)O_2	cubic	**primary**	Gd0.26Zr0.74O1.87	04-017-4773
YSZ–HfO_2	**YSZ**	tetragonal	**primary**	Zr0.92Y0.08O1.96	00-048-0224
	HfO_2	monoclinic	minor	HfO2	00-072-0468

Note: Primary phase observed in each spectrum is bolded.

The top surface of the coatings was polished to examine the microstructure of the coatings (Fig. 14). The YSZ coating (Fig. 14a) shows a typical dense vertically cracked structure with a few regions of porosity due to unmelted particles. The YSZ–CeO_2 and YSZ–Sm_2O_3 coatings also have large regions of cracking as well as many regions of unmelted particles causing significant porosity in the coating. A dense phase (white particles) is found within some of the porous regions of both coatings (see Figs. 14b and 14c, respectively). The YSZ–Gd_2O_3 coating (Fig. 14d) also has large cracking and porous regions but no dense secondary phase. The YSZ–HfO_2 coating has fewer large cracking regions but many porous regions. A lower-density phase, likely YSZ, was found uniformly dispersed in all the YSZ–REO coatings. Figure 14f shows the darker gray phase in a higher magnification micrograph of the YSZ–CeO_2 coating. Since this phase is uniformly distributed and has an isotropic morphology, it is suspected to have precipitated while the coating was solidifying and/or cooling.

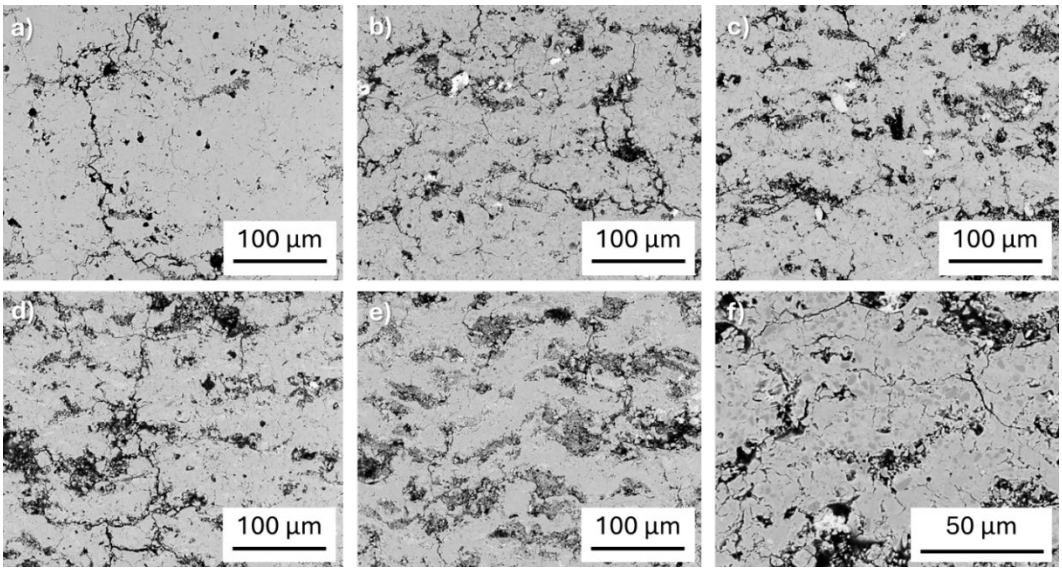

Fig. 14 SEM backscattered electron micrographs of the polished top surface of the YSZ and YSZ–REO coatings: a) YSZ, b) YSZ–CeO_2, c) YSZ–Sm_2O_3, d) YSZ–Gd_2O_3, e) YSZ–HfO_2, and f) YSZ–CeO_2 at higher magnification

Figure 15 shows the porosity of each coating. Porosity from unmelted particles were found in all coatings, but it is expected that the larger particle size of the experimental YSZ–REO powders (see Table 2) resulted in more unmelted particles—in this case roughly doubling the resultant porosity compared to the YSZ coating. In addition, some of the powder particles were visibly hollow (see Fig. 1), which has proven previously to incorporate porosity into APS coatings.[17] If desired, a denser coating could be produced by adjusting the APS processing conditions. Changing the APS plasma chemistry to an Ar–H_2 could reduce the plasma viscosity (increase plasma velocity resulting in faster moving molten particles) and increase the thermal conductivity of the plasma (better heat transfer to particles).[18] A more effective melting of the particles could be achieved by increasing the powder residence time in the plasma plume by either reducing the carrier gas flow rate or by increasing the plasma enthalpy through increasing plasma power. Or producing a powder with a finer particle size would also enable more rapid melting of the powder resulting in a denser coating.

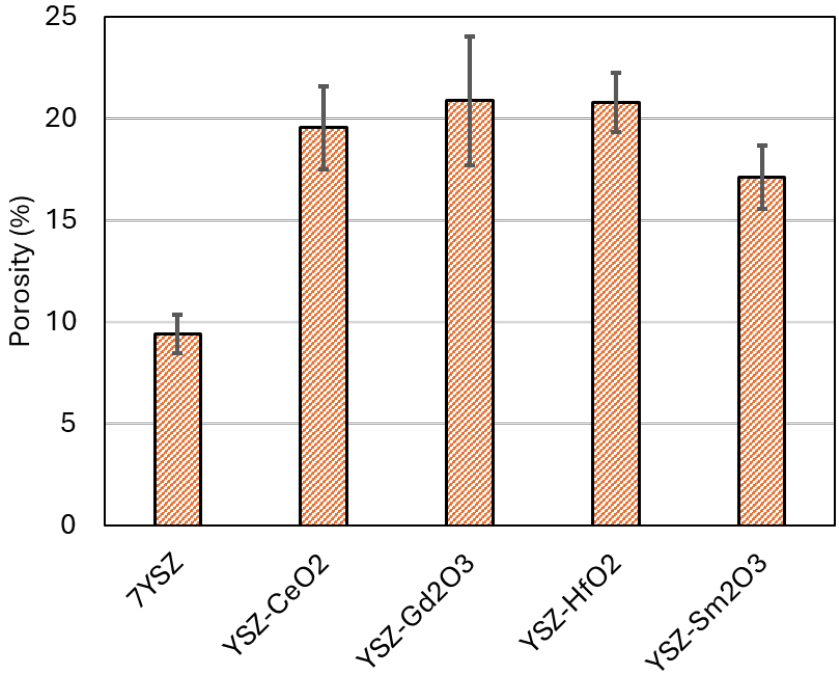

Fig. 15 Comparison of porosity for the YSZ and YSZ–REO coatings

3.3 Coating-CMAS Behavior

The wettability of CMAS for the YSZ–CeO_2, YSZ–Gd_2O_3, and YSZ–Sm_2O_3 coatings was reported elsewhere[18] and will only be summarized here. The YSZ–HfO_2 coating was not evaluated for CMAS interaction. In the work by Wright et al.,[19] the wettability of the YSZ–REO coatings was compared to polished and sintered pellets made from the powders, assuming the chemistry to be similar with the goal of isolating the chemistry effect on CMAS behavior from the surface roughness and microstructure effects. The coating porosity was similar for all the YSZ–REO coatings tested and was therefore neglected in this analysis. The contact angle of a molten CMAS droplet was measured as a function of time while the sample was held at 1260 °C, which is above the melting point of the CMAS used. For YSZ, increasing the surface roughness and porosity resulted in a smaller CMAS contact angle than in the polished pellet case, which was attributed to the CMAS infiltrating the rough surface of the YSZ and therefore reducing the spreading rate. The pellets and coatings containing REO reacted with the CMAS, forming a sealing layer. For the YSZ–REO samples, the increase in roughness resulted in an increase in spreading rate.

In the original YSZ–Gd_2O_3 blended work, it was suspected that the direct interaction between the CMAS and Gd_2O_3 layers caused the formation of a "weak interface," which spalled during cooling.[10] In the work by Wright et al.,[19] the CMAS interaction with YSZ–Sm_2O_3 was examined in detail as a case study,

supposing that the other coatings behaved similarly. For this coating, the CMAS bonded well, forming an apatite phase that adhered after cooling. The predominant phase in the tested YSZ–REO coatings was the fluorite, $(REO,Zr)O_2$, phase. While this chemistry still has the propensity to react with the CMAS to form apatite, the reaction growth rate appears to be higher than what was observed previously,[10] which may be the reason for the enhanced CMAS adhesion.

The spreading rate, dCA/dt, from the contact angle measurements provides a quantitative measurement of the kinetics of the droplet spreading across the surface as well as provides insight on the interaction of the CMAS with the material being tested. The difference in optical basicity, $\Delta\Lambda$, between the CMAS and the tested chemistry has been previously correlated with CMAS behavior, where a larger $\Delta\Lambda$ results in higher CMAS reactivity.[20] The spreading rate plotted against optical basicity for the YSZ and YSZ–REO pellets and coatings is provided in Fig. 16 (data from Wright et al.[19]). There is significant scatter in the data but if circles are added identifying the primary phase, some trends may be found. There are not enough data points in the YSZ or YSZ–REO circle to make any solid conclusions, but it is interesting to note that the YSZ–HfO_2 pellet has the smallest $\Delta\Lambda$, indicating least reactive with CMAS, yet had a much slower spreading rate than the pure YSZ pellet. Clearly, the presence of HfO_2 in the coating reduced the CMAS spreading compared to YSZ alone. Quite a few of the YSZ–REO pellets and coatings formed a fluorite phase. There is still limited data but if the trend can be believed, higher optical basicity change increases the CMAS spreading rate. The YSZ–CeO_2 sample, which had the lowest $\Delta\Lambda$ of the coatings consisting of primarily fluorite, had the highest resistance to CMAS spreading. If this relation holds true for other rare-earth containing fluorites, it may be possible to design a chemistry with near-zero spreading (perhaps even sand-phobic?) by finding a REO with a lower optical basicity than YSZ–CeO_2 that still forms a fluorite phase.

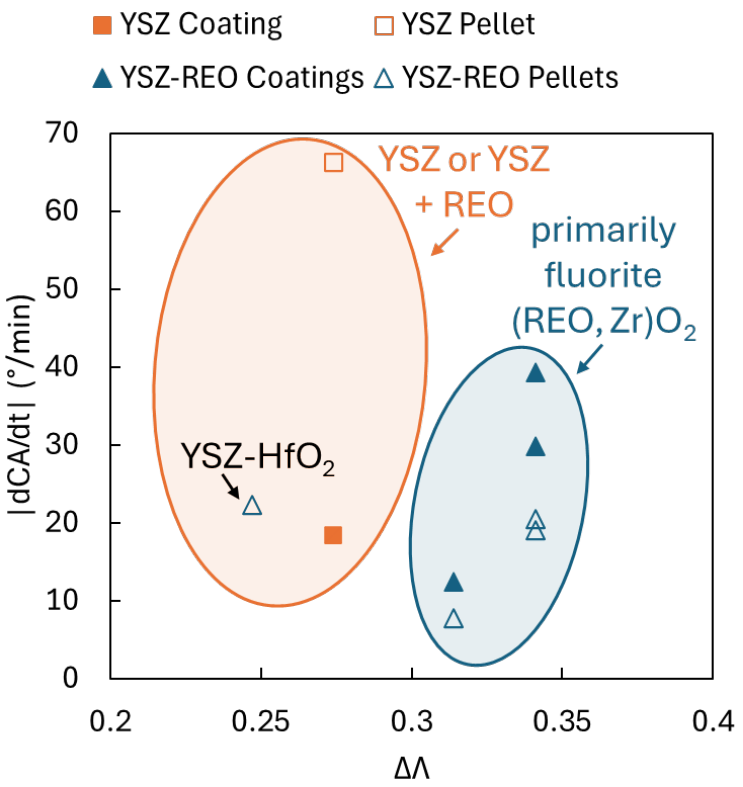

Fig. 16 Rate of spreading as a function of optical basicity difference from CMAS

4. Conclusion

This study attempted to validate the previously observed CMAS and YSZ–Gd_2O_3 lack of adhesion behavior using a more robust, easier-to-process APS powder. Other YSZ–REOs (Sm_2O_3, CeO_2, and HfO_2) were also manufactured to evaluate trends for processability and coating-CMAS behavior. YSZ–REO powders with improved processability were created using a spray drying and sintering route. These YSZ–REO powders had a larger particle size than the commercial YSZ powders used previously, which resulted in higher coating porosities using the same APS processing conditions. The better mixing and smaller particle size of the YSZ–REO particulates resulted in reaction of the YSZ with the REO during the powder sintering process and continued during APS processing, forming a cubic fluorite phase for all but the YSZ–HfO_2 chemistry. Agglomerating and sintering the REO separate from the YSZ and then blending prior to APS may enable the deposition of separate, banded coatings, which were observed in previous work,[10] but with enhanced processability. The YSZ–HfO_2 chemistry remained separate during both sintering and APS; however, significant HfO_2 phase was lost during APS resulting in a primarily YSZ coating. CMAS behavior was evaluated for all coatings except the YSZ–HfO_2 coating via contact angle methods reported elsewhere.[19] The REO reacted with CMAS to form an apatite phase that sealed the coating from further

infiltration. This sealing behavior resulted in increased spreading of the CMAS with increasing surface roughness. Differing CMAS wettability between the pellets and coatings may be a combined result of both the surface roughness (pellets were polished) but also microstructure. Polishing the as-sprayed coatings may provide additional understanding of the effect of microcracks and porosity on the wettability of CMAS.

5. References

1. Padture NP, Gell M, Jordan EH. Thermal barrier coatings for gas-turbine engine applications. Science. 2002;296:280–284.

2. Perepezko JH. The hotter the engine, the better. Science. 2009;326:1068–1069.

3. Levi CG, Hutchinson JW, Vidal-Setif M-H, Johnson CA. Environmental degradation of thermal-barrier coatings by molten deposits. MRS Bulletin. 2012;37(10):932–941.

4. Krämer S, Yang J, Levi CG. Infiltration-inhibiting reaction of gadolinium zirconate thermal barrier coatings with CMAS melts. J Am Ceram Soc. 2008;91(2):576–583.

5. Poerschke DL, Barth TL, Levi CG. Equilibrium relationships between thermal barrier oxides and silicate melts. Acta Materialia. 2016;120:302–314.

6. Poerschke DL, Levi CG. Effects of cation substitution and temperature on the interaction between thermal barrier oxides and molten CMAS. J Eur Ceram Soc. 2015;35(2):681–691.

7. Cao G, Wang S-Q, Wang Y-H, Ding Z-Y, Liu Z-G, Ouyang J-H, Wang Y-M, Wang Y-J. Growth kinetics of apatite layer evolved from calcia–magnesia–aluminosilicate (CMAS) hot corrosion reaction of (Y1-Yb)2SiO5 ceramics at elevated temperatures of 1673 K and 1773 K. J Eur Ceram Soc. 2023;43(2):600–611.

8. Vaben R, Traeger F, Stover D. New thermal barrier coatings based on pyrochlore/YSZ double-layer systems. Appl Ceram Technol. 2004;1(4):351–361.

9. Mahade S, Curry N, Björklund S, Markocsan N, Nylén P, Vaßen R. Erosion performance of gadolinium zirconate-based thermal barrier coatings processed by suspension plasma spray. J Therm Spray Technol. 2017;26(1–2):108–115.

10. Mock C, Walock MJ, Ghoshal A, Murugan M, Pepi M. Adhesion behavior of calcia–magnesia–alumino–silicates on gadolinia–yttria-stabilized zirconia composite thermal barrier coatings. J Mater Res. 2020;35(17):2335–2345.

11. Mock C, Sotiropoulos N. Addendum to ARL-TR-9992, improved yttria-stabilized zirconia (YSZ) and rare earth oxide (REO) blends: processability and calcia–magnesia–alumina–silicate response. DEVCOM Army Research Laboratory (US); 2024 Oct. Report No.: ARL-TN-1231. (Report is CUI).

12. Schindelin J, Arganda-Carreras I, Frise E, Kaynig V, Longair M, Pietzsch T, Preibisch S, Rueden C, Saalfeld S, Schmid B, et al. FIJI: an open-source platform for biological-image analysis. Nat Methods. 2012;9:676–682.

13. Alqallaf J, Teixeira JA. Blade roughness effects on compressor and engine performance—A CFD and thermodynamic study. Aerospace. 2021;8(11).

14. Swain BK, Mohapatra SS, Pattanaik A, Samal SK, Bhuyan SK, Barik K, Sahoo D, Behera A. Sensitivity of process parameters in atmospheric plasma spray coating. J Therm Spray Eng. 2018;1(1):1–6.

15. Wang C, Zinkevich M, Aldinger F. Phase diagrams and thermodynamics of rare-earth-doped zirconia ceramics. Pure Appl Chem. 2007;79(10):1731–1753.

16. Zhang F, Chen C-H, Hanson JC, Robinson RD, Herman IP, Chan S-W. Phases in ceria–zirconia binary oxide $(1-x)CeO_2$–$xZrO_2$ nanoparticles: the effect of particle size. J Am Ceram Soc. 2005;89(3):1028–1036.

17. Guo HB, Murakami H, Kuroda S. Effect of hollow spherical powder size distribution on porosity and segmentation cracks in thermal barrier coatings. J Am Ceram Soc. 2006;89(12):3797–3804.

18. Fauchais PL, Heberlein JVR, Boulos MI. Thermal plasmas used for spraying. In: Thermal spray fundamentals: from powder to part. Springer New York; c2014. p. 84–95.

19. Wright AJ, Kim Y, Mock C, Sharobem T, McGowan R, Bravo L, Murugan M, Dambra C, Keyes B, Ghoshal A. Influence of chemistry and surface roughness of various thermal barrier coatings on the wettability of molten sand. Surf Coat Technol. 2024;481:130649.

20. Tian Z, Zhang J, Zheng L, Hu W, Ren X, Lei Y, Wang J. General trend on the phase stability and corrosion resistance of rare earth monosilicates to molten calcium–magnesium–aluminosilicate at 1300 °C. Corros Sci. 2019;148:281–292.

List of Symbols, Abbreviations, and Acronyms

APS	air plasma spray
ARL	Army Research Laboratory
CeO_2	cerium oxide
CMAS	calcia–magnesia–alumina–silicate
Cu	copper
DEVCOM	US Army Combat Capabilities Development Command
Gd_2O_3	gadolinium oxide
HfO_2	hafnium oxide
ID	identification
N/A	not applicable
PDF	powder diffraction file
PFT	powder flow tester
REO	rare-earth oxide
rpm	revolutions per minute
SE	secondary electron
SEM	scanning electron microscopy
SERDP	Strategic Environmental Research and Development Program
Sm_2O_3	samarium oxide
vol%	percentage by volume
wt%	weight percent
XRD	X-ray diffraction
Y_2O_3	yttrium oxide
YSZ	yttria-stabilized zirconia
ZrO_2	zirconium dioxide

1 (PDF)	DEFENSE TECHNICAL INFORMATION CTR DTIC OCA
1 (PDF)	DEVCOM ARL FCDD RLB CI TECH LIB